Accepted Article

Authors: Can Guo, Jie Zhou, Yuting Chen, Huifen Zhuang, Qi Li, Jie Li, Xi Tian, Yuluan Zhang, Xiaoman Yao, Yifa Chen, Shun-Li Li, and Ya-Qian Lan

RESEARCH ARTICLE

Synergistic Manipulation of Hydrogen Evolution and Zinc Ion Flux in Metal-Covalent Organic Frameworks for Dendrite-free Zn-based Aqueous Batteries

Can Guo[a]‡, Jie Zhou[a]‡, Yuting Chen[a], Huifen Zhuang[a], Qi Li[b], Jie Li[a], Xi Tian[b], Yuluan Zhang[a], Xiaoman Yao[a], Yifa Chen[a]*, Shun-Li Li[a] & Ya-Qian Lan[a]*

[a]   Dr. C. G., J. Z., Y. C., H. Z., Y. Z., X. M., Prof. Y. C., Prof. S.-L. L. and Prof. Y.-Q. L.
       School of Chemistry
       National and Local Joint Engineering Research Center of MPTES in High Energy and Safety LIBs, Engineering Research Center of MTEES (Ministry of Education), and Key Lab. of ETESPG (GHEI)
       South China Normal University
       Guangzhou, 510006, P. R. China
E-mail: chyf927821@163.com; E-mail: yqlan@njnu.edu.cn; yqlan@m.scnu.edu.cn
[b]   Dr. Q. L. and X. T.
       School of Chemistry and Materials Science
       Nanjing Normal University
       Nanjing 210023, P. R. China
       Homepage : http://www.yqlangroup.com/

       ‡ Can Guo and Jie Zhou contributed equally to this work

       Supporting information for this article is given via a link at the end of the document.

Abstract: Zn-based aqueous batteries have attracted much attention because of their high theoretical-capacity, safety, and low-cost, yet the H_2-evolution, qualification or inhibition mechanism investigations that are closely related to the dendrite-growth are rare and challenging. Herein, a series of zincophilic metal-covalent organic frameworks (e.g., Zn-AAn-COF, Zn-DAAQ-COF, and Zn-DAA-COF) have been explored as model-platforms to manipulate the H_2-evolution and Zn^{2+} flux. Best of them, Zn-AAn-COF based cell only produces 0.002 mmol h^{-1} cm^{-2} H_2, which is > 2 orders of magnitude lower than bare Zn. Noteworthy, it affords high stability for 3000 cycles (overpotential, < 79.1 mV) at 20 mA cm^{-2} in symmetric-cell and enhanced cycling-stability up to 6000 cycles at 2000 mA g^{-1} in the assembled full-battery. Besides, mechanistic characterizations show that Zn-AAn-COF can enhance the energy-barrier of H_2-evolution and homogenize the ion-distribution or electric-filed to achieve high performance.

Introduction

Zn-based aqueous batteries (ZABs) have been considered as the promising electrochemical energy storage systems to replace the state-of-the-art dangerous/expensive Li-ion batteries.[1] Since its appearance in the very first battery invented by Alessandro Volta Pile in 1799, metallic Zn has been believed as an ideal anode material for aqueous ZABs stemming from its high theoretical capacity (820 mAh g^{-1}), low electrochemical potential (-0.76 V *vs* standard hydrogen electrode), abundant resource, and low toxicity.[2] Nonetheless, the development of ZABs still faces great obstructions, as exemplified by their uncontrolled formation of Zn dendrite and detrimental parasitic reactions (e.g., H_2 evolution reaction).[3] In particular, Zn metal in aqueous solution environments is thermodynamically unstable, thus the reduction of Zn^{2+} is continuously interfered by the H_2 evolution through the decomposition of H_2O (Zn + $2H_2O$ → $Zn(OH)_2$ + H_2) due to the relatively low H_2-forming energy barrier, which inevitably induce the unsatisfactory spontaneous side reactions

or electrolyte consumption.[4] Subsequently, these by-products formation unavoidably diminishes the Zn utilization and cycling life, enhances the contact surface area between electrolyte and Zn anode, and in turn contributes to the inhomogeneous Zn^{2+} flux distribution, which would fascinate mushrooming Zn^{2+} flux and result in Zn protrusions. In addition to these issues, the protruding regions with disordered, loose, and brittle Zn dendrites deliver a strong concentrated electric field, where H_2 evolution is more exuberant and might cause a rapid increase of internal pressure of the airtight batteries or quick electrolyte consuming, directly leading to safety concerns (e.g., electrolyte leakage and explosion) and early short-circuit of the batteries.[4b,5]

Up to now, some promising materials, such as anti-corrosion elastic constraint (AEC), polyimide coating, ZnF_2 layer, In layer, Sb layer, and Zn-alloy, have attracted tremendous interest and developed as the interfacial modification layers for ZABs to inhabit detrimental parasitic reactions.[4b,6] However, some challenging issues like the huge volume change during the Zn plating/stripping processes, hardly uncontrolled Zn diffusion/de-solvation kinetics, parasitic reactions with abundant H_2 bubble generation make it a giant challenge to design mechanically strong protective layers to meet the multi-requirements of potential practical applications. Among them, the long-neglected issues of H_2 evolution still require intensively research, especially for the quantifying and deep-understanding of the H_2 evolution mechanisms on the electrode during the Zn deposition, which also play a vital role in studying the factors related to capacity loss and battery failure.[7] Besides, the traditional coating of protective layers onto Zn anode would inevitably increase the additional porosity and weight of the cell, thereby reducing the volumetric/gravimetric energy density for the batteries. Therefore, the design of powerful protective layers with desired multi-functionality that can inhibit both side reactions (e.g., H_2 evolution) and Zn corrosion to achieve high-performance ZABs is much preferred yet largely unmet.

Covalent organic frameworks (COFs), as an emerging class of crystalline and porous polymeric materials with light-weight, high porosity, structural tunability, and high chemical stability, have

RESEARCH ARTICLE

been widely investigated regarding catalysis, energy storage, adsorption and separation, optoelectronics, etc.[8] Unlike traditional amorphous organic polymers, COFs can predictably organize redox-active groups and provide porous host platforms to be applied in ZABs.[9] In this respect, it is speculated that the applications of COFs in this field can be attributed to the advantages: 1) the designable structures of COFs can rationally select the construction struts with functional groups like polar or zincophlic ones (e.g., -C=O, -SO₃, -NH₂, -S-, and -CF₃, etc.) to provide high interactions with Zn²⁺, water molecules, and Zn surface to facilitate the generation of zincophilic layer, electrolyte/electrode wetting and Zn²⁺ hopping/deposition,[10] 2) the large surface area of COFs would reduce the local current density to effectively homogenize the distribution of Zn²⁺ flux and space electric field, thus accelerating the Zn deposition kinetics and preventing H₂ formation,[11] and 3) COFs with high porosity and light-weight would serve as attractive host platforms to maximize the active sites while maintaining the high volumetric/gravimetric energy density. Accordingly, the modification of Zn anode with COFs layers might be potential alternatives to conquer the above-mentioned challenges of ZABs.[4b,12] Up to date, only a few works have applied COFs (i.e. FCOF, TpPa-SO₃H COF and DIP D) in ZABs as anode protective layers,[11b,13] and the quantification or mechanistic study of H₂ evolution remain as a daunting challenge as far as we know. In this context, an elaborate design of electrochemically active COFs based protective layers that can synergistically manipulate the H₂ evolution and Zn²⁺ flux to achieve ultralong cycling stability, high energy density, and large power density is imperative and feasible.

In this work, we have developed a series of zincophilic COFs (i.e. Zn-AAn-COF, Zn-DAAQ-COF, Zn-DAA-COF) as model platforms to manipulate the H₂ evolution and Zn²⁺ flux in ZABs (Figure 1). Density functional theory (DFT) calculations results show that the zincophilic COFs like Zn-AAn-COF has a higher adsorption energy for Zn atoms than that of Zn foil, indicating it has better Zn affinity and the unique pore structure and electrostatic potential distribution of Zn-AAn-COF can effectively remove the Zn solvated water in the bulk electrolyte.[4b,6e,7,14] Specifically, H₂ evolution has been successfully qualified and studied in these COFs based model platforms. Best of them, Zn-AAn-COF based cell only produces 0.002 mmol h⁻¹ cm⁻² H₂, which is > 2 orders of magnitude lower than that of bare Zn cell. In addition, the PVC-Zn-AAn-COF@Zn anode can work smoothly even at a high current density of 20 mA cm⁻² over 3000 cycles with low overpotential (~79.1 mV) in symmetric cells. Additionally, its lifespan is nearly 16 times than bare Zn cell and the average Coulombic efficiencies (CE) value at 20 mA cm⁻² is as high as 98.7%. When paired with MnO₂ cathode, the full cell can exhibit excellent cycle stability (discharge capacity, 217.2 mAh g⁻¹) at 200 mA g⁻¹, far outperforming Zn//MnO₂ (discharge capacity, 123.9 mAh g⁻¹) under similar conditions. Besides, H₂ inhibition and Zn dendrite formation have been intensively studied by DFT calculations and sufficient characterizations, which deliver that these COFs can enhance the energy-barrier of H₂ evolution and homogenize the ion-distribution or electric-filed to achieve high performances.
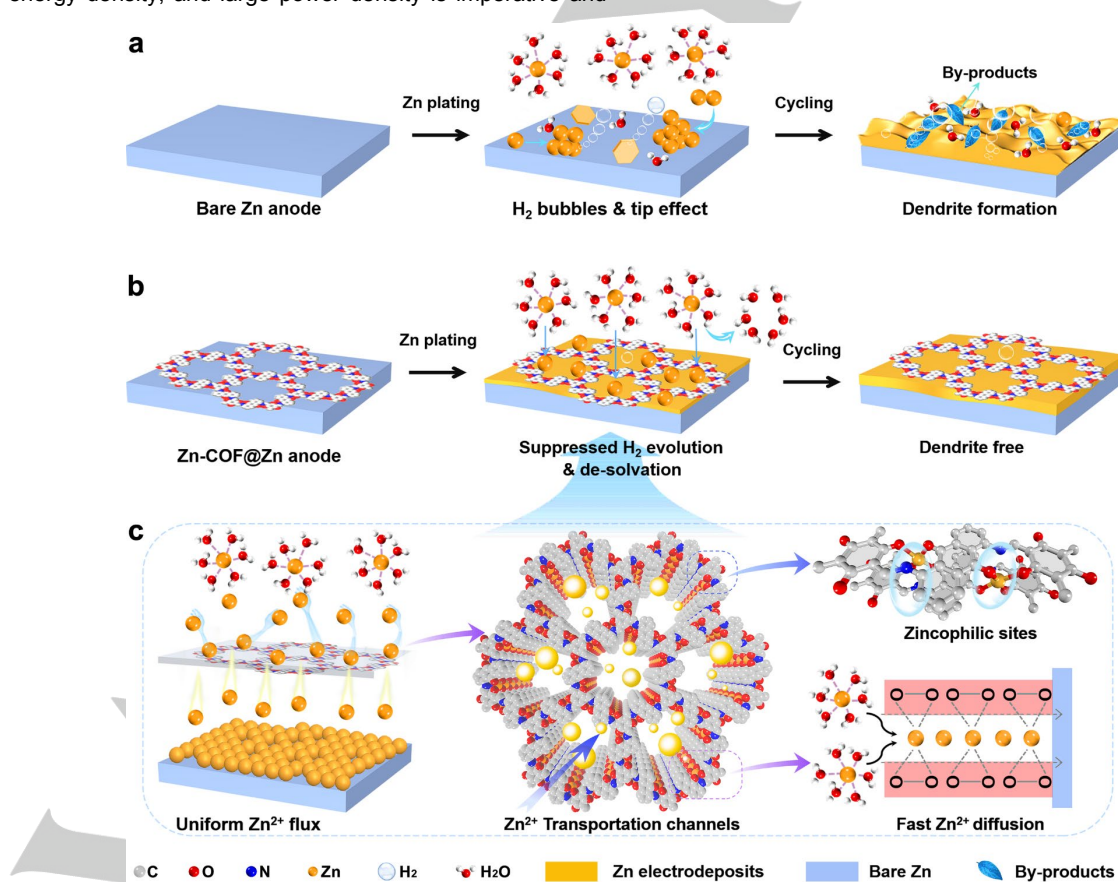

Figure 1. The structure design and mechanism elucidation of Zn-COF@Zn anode. (a) Schematic comparison of Zn deposition process on bare Zn surface. (b, c) Schematic presentation of Zn deposition process on Zn-COF@Zn surface.

2

RESEARCH ARTICLE

Results and Discussion

To better demonstrate the role of different components in suppressing hydrogen evolution and dendrite growth, Zn-AAn-COF, Zn-DAAQ-COF, and Zn-DAA-COF are synthesized by direct metalation of COFs with zinc acetate through a simple hydrothermal method (Figure 1a and S1, details see Methods).[4b,15] Fourier-transform infrared (FT-IR) spectra have been performed reveal the chemical component (Figure S2-S4). Taking Zn-AAn-COF as an example, the generated β-ketoenamine is observed at 1250 and 1564 cm^{-1}, assigned to -C-N and -C=C stretching bands (Figure S2). [15a,15b] This result is further verified by ^{13}C cross-polarization magic-angle-spinning solid-state nuclear magnetic resonance (^{13}C CP-MAS NMR) spectroscopy. The signals at 145 and 120 ppm are attributed to the enamine carbon (=C-N-H) and α-enamine carbon of β-ketoenamine, respectively (Figure S5).[15a] The crystal structure of the as-synthesized COFs throughout the network is identified by powder X-ray diffraction (PXRD) measurement. For instance, the PXRD pattern of Zn-AAn-COF matches with that of AAn-COF, and the sharp diffraction peaks demonstrate high crystallinity. The PXRD pattern of Zn-AAn-COF manifests diffraction peaks at 4.1°, 7.1°, 8.2°, 10.8° and 12.2°, which correspond to (100), (210), (200), (310) and (300) crystal planes, respectively (Figure S6). Besides, no additional peaks appear and the only observable change of Zn-AAn-COF is the slightly decreased intensity of peaks, confirming the retention of AAn-COF structure. In addition, the metalation procedures used for DAAQ-COF, and DAA-COF are the same as that of AAn-COF and the corresponding structures are confirmed by the PXRD patterns (Figure S7 and S8). The porosity and Brunauer-Emmett-Teller surface area (S_{BET}) have been examined by N_2 adsorption-desorption measurements at 77 K (Figure S9, S10 and Table S1). The S_{BET} of AAn-COF is calculated to be 321 m^2 g^{-1}, which decreases to 279 m^2 g^{-1} after the loading of Zn. Besides, the pore size distribution (~1.2 nm) of Zn-AAn-COF displays lower value than the pore size distribution before Zn^{2+} loading (insert, Figure S9). The relative N_2 sorption results of the contrast samples (i.e. Zn-DAAQ-COF and Zn-DAA-COF) are calculated and they also demonstrate porous structures.

At the same time, high-resolution X-ray photoelectron spectroscopy (XPS) measurements have been analyzed to further verify the successful loading of Zn^{2+} into COFs. For example, the observed binding energies of 1021.8 eV and 1045.8 eV are ascribed to Zn 2p$_{3/2}$ and Zn 2p$_{1/2}$ for Zn-AAn-COF (Figure S11), respectively.[15a] Besides, the fine O 1s XPS spectrum of Zn-AAn-COF presents the existence of Zn-O bonds (Figure S12).[15a,15c] These results stem mainly from the coordination interaction between Zn^{2+} and carbonyl group of AAn-COF. Moreover, the XPS results of Zn-DAAQ-COF display a similar trend after the Zn^{2+} modification, which proves the successful preparation of Zn-DAAQ-COF (Figure S15). However, the XPS measurement of Zn-DAA-COF has also been analyzed and the results reveal no relative spectrum of Zn^{2+}, which implies the weak coordination interaction for DAA-COF when compared with AAn-COF and DAAQ-COF (Figure S16). As expected, the total Zn content of Zn-AAn-COF is determined to be 9.21 wt% by inductively coupled plasma optical emission spectrometry (ICP-OES) tests, which is higher than Zn-DAAQ-COF (7.27 wt%) and Zn-DAA-COF (0.65 wt%) (Table S2). On the basis of the results

of Zn content, the coordination number of Zn^{2+} in AAn-COF (~2) and DAAQ-COF (~1.5) are less than the theoretical number of Zn^{2+} (6). The existence of -C=O moieties in AAn-COF and DAAQ-COF are principally responsible for the storage of Zn^{2+}.[16] In addition, we have performed DFT calculations to confirm the atomic configuration evolution of AAn-COF, DAAQ-COF, and DAA-COF after Zn^{2+} modification (Figure S17-19). Due to Zn^{2+} can coordinate with organic substances of O or N,[15c] we considered various possible binding sites to identify the defined coordination sites. Taking AAn-COF as an example, there are three possible sites including two kinds of carbonyl groups in Tp and AAn ligands, respectively, and -C=N that can coordinate to Zn^{2+} from both inner- and inter-layer. We firstly studied the possible interactions of the three sites in the inner-layer to interact with Zn^{2+} and found no stable bonds could be generated for all of them (Figure S17a). Even more, the bonding is also weak for interaction mode with one carbonyl group from adjacent inter-layer (-0.104 eV). After calculation, the favorable configuration of AAn-COF with strong interaction (adsorption energy, -1.44 eV) is bonding one Zn^{2+} to four carbonyl groups, in which each two carbonyl groups are from adjacent inter-layer. For DAAQ-COF, the distance of adjacent carbonyl groups in the inner-layer is longer than the suitable one for Zn^{2+} coordination and only two carbonyl groups from adjacent inter-layer are coordinated to Zn^{2+}, thus leading to relatively weaker adsorption energy (-0.230 eV). Interestingly, DAA-COF with similar coordination mode of DAAQ-COF possesses much lower adsorption energy (-0.15 eV), possibly attributed to the special configuration of DAA ligand in the structure when compared to that of AAn and DAAQ. The calculations result match well with the Zn content results aforementioned.

To characterize the morphology of the synthesized samples, scanning electron microscopy (SEM) and transmission electron microscopy (TEM) tests have been further conducted. Taking Zn-AAn-COF for instance, SEM images display that the nanofiber morphology has average diameter of ~50 nm and length of ~2.0 μm, which matches with that of AAn-COF (Figure S20 and S21).[15a,15b] In comparison, Zn-DAAQ-COF and Zn-DAA-COF all present accumulated nanoparticle morphology (particle size, ~100 nm) in the SEM tests (Figure S22 and S23). Besides, the high-resolution transmission electron microscopy (HRTEM) images clearly show the lattice fringes of Zn-AAn-COF with a spacing of ~2.1 nm, corresponding to the reflections from the (100) lattice planes at 4.1° diffraction peak (Figure S24a). Energy-dispersive X-ray spectroscopy (EDS) mapping spectrum reveals that C, N, O, and Zn elements are uniformly distributed in Zn-AAn-COF (Figure S24b).

Based on the above-mentioned results, we have obtained three kinds of COFs with high porosity, zincophilic groups (e.g., -C=N and -C=O) and Zn nucleation sites, which might serve as ideal model platforms for the study of ZABs. To investigate the battery property, the electrode has been fabricated by drop casting COFs based polyvinyl chloride (PVC) suspension onto the surface of Zn plates followed by slow evaporation of solvent (detail see Method). The PVC-Zn-AAn-COF displays uniform morphology when compared with that of bare PVC film (Figure S25 and S26). The side-view image presents that the PVC-Zn-AAn-COF is tightly anchored onto Zn surface with a thickness of ~5 μm (Figure S25a). Meanwhile, PVC-Zn-DAAQ-COF and PVC-Zn-DAA-COF are also prepared and characterized by the SEM tests (Figure S29). In addition, the polar functional groups of the coating can
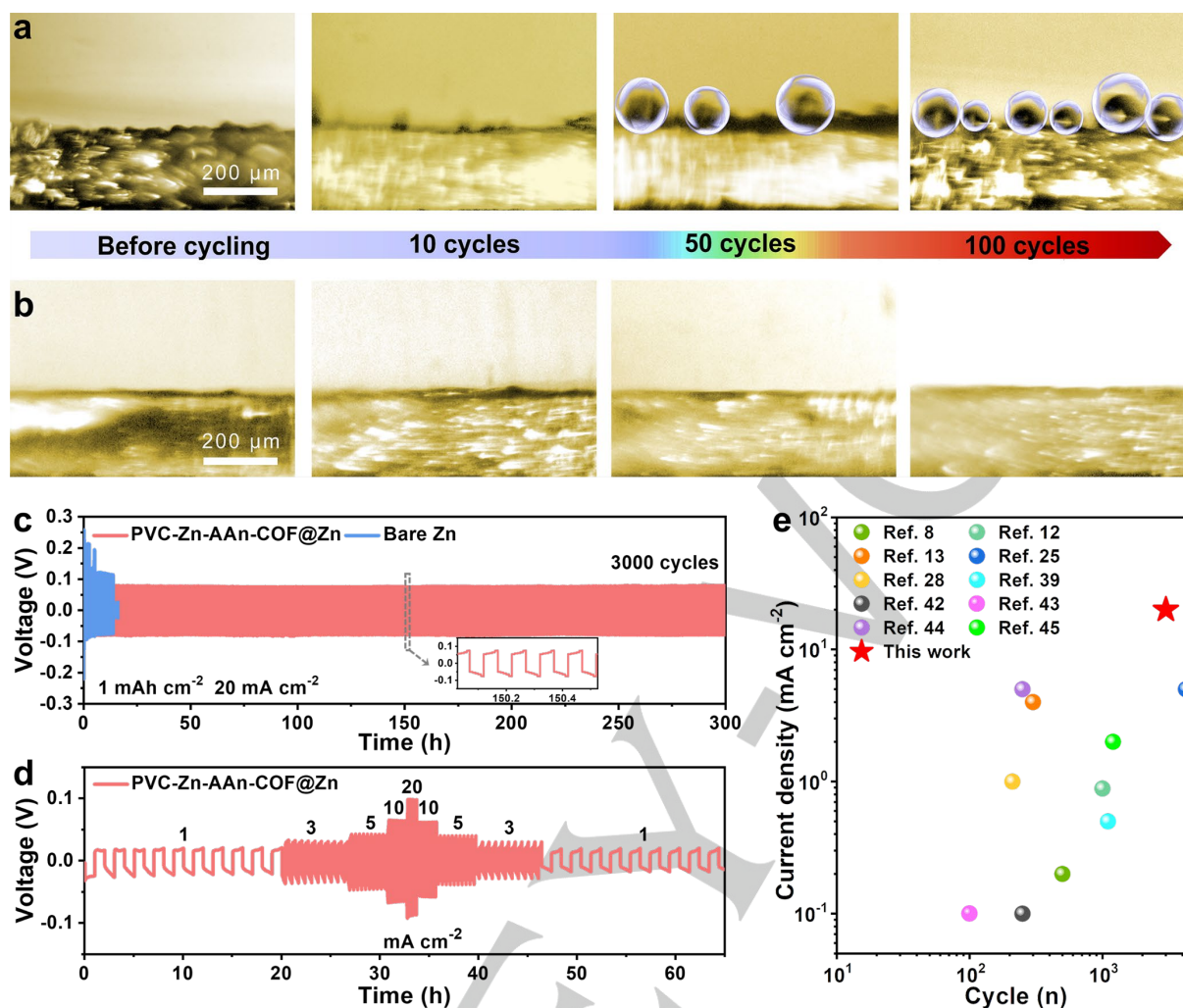
3

RESEARCH ARTICLE

Figure 2. *In-situ* operando optical microscope images of Zn plating behavior and the electrochemical performance of for different electrodes. (a, b) Bare Zn and PVC-Zn-AAn-COF@Zn during plating/stripping at 20 mA cm^{-2}. (c) Comparative cycling stability of symmetrical cells using PVC-Zn-AAn-COF@Zn anode and bare Zn foil at current density of 20 mA cm^{-2} with a capacity of 1 mAh cm^{-2} (insert image, the circled place in c). (d) Rate capability of symmetrical cells assembled using PVC-Zn-AAn-COF@Zn anode at various current densities from 1 to 20 mA cm^{-2}. (e) Comparison of the life-span of symmetrical cells with PVC-Zn-AAn-COF@Zn anode with previously reported Zn composite anodes under different current densities.

significantly improve the hydrophilic surface affinity of zinc foil (Figure S30). To examine the corrosion resistance of PVC-Zn-AAn-COF, we soaked the Zn foil with and without PVC-Zn-AAn-COF layer into 1 M ZnSO$_4$ electrolyte. As shown in Figure S31, the shiny smooth surface of bare Zn foil turns bright to gray and is seriously corroded with the detected rough and uneven surface after 7 days. In contrast, the change of PVC-Zn-AAn-COF@Zn surface is negligible after similar treatment. In addition, the excellent adhesion property of PVC-Zn-AAn-COF has been verified by the twisting experiments, which reveals that it has strong adhesion to the Zn foil (Figure S32).[6d,17] Furthermore, the digital photograph of the PVC-Zn-AAn-COF@Zn electrode after repeated adhesion for 100 times further support the above view (Figure S33).

To directly prove the restrained H$_2$ evolution on the PVC-Zn-AAn-COF@Zn electrode, *in-situ* optical microscope monitoring the Zn plating/stripping behavior in transparent symmetrical cell (current density, 20 mA cm^{-2} and capacity, 1 mAh cm^{-2}) has been conducted.[11b,18] After 10 cycles, the protrusions or nucleations

begin to grow along on the surface and edges of the bare Zn foil, and they gradually transform into Zn dendrites on the Zn foil with increasing cycles, indicating the inhomogeneous Zn plating (Figure 2a).[18] Quite uneven Zn deposition, abundant H$_2$ bubbles and severe corrosion are observed at 100 cycles for bare Zn foil (Figure 2a). In strong comparison, the surface of PVC-Zn-AAn-COF@Zn foil is smooth before cycling under the same conditions (Figure 2b). Even after 100 cycles during plating/stripping process, it exhibits uniform and compact Zn deposition with no H$_2$ bubbles or sign of dendrites during cycling (Figure 2b). Moreover, the Zn plating behaviors on PVC-Zn-AAn-COF@Zn electrodes are investigated by using 2032-type coin cells with 1 M ZnSO$_4$ electrolyte. SEM images of PVC-Zn-AAn-COF@Zn after plating at 20 mA cm^{-2} exhibit smooth surface without any cumulation of Zn (Figure S34). Due to the de-solvation and nucleophilic induction effect, PVC-Zn-AAn-COF@Zn shows a lower nucleation overpotential and a gentle deposition curve (Figure S35). Furthermore, the effects of PVC-Zn-AAn-COF@Zn anodes on H$_2$ evolution are evaluated by linear sweep voltammetry (LSV)

4

RESEARCH ARTICLE

and the onset potential for H_2 evolution on Zn-AAn-COF electrode is higher than that on Zn electrode (Figure S36).[5a,18]

In addition, the stability of bare Zn and PVC-Zn-AAn-COF@Zn anodes has been evaluated by the long-term galvanostatic cycling (Figure 2c and S37). The bare Zn symmetrical battery displays an abrupt decrease of the polarization voltage after 279 cycles at 10 mA cm^{-2}. In contrast, the PVC-Zn-AAn-COF@Zn symmetrical cell reveals fantabulous cycling stability over 1500 cycles (Figure S37c). Besides, cells based on PVC-AAn-COF@Zn, PVC-Zn-DAAQ-COF@Zn and PVC-Zn-DAA-COF@Zn anodes present casual voltage oscillations with abrupt decrease or significant increase in polarization voltage after ~64, ~130 and ~30 h plating/stripping at 10 mAh cm^{-2}, respectively (Figure S38-40). Even though the current density is increased to 20 mA cm^{-2}, the PVC-Zn-AAn-COF@Zn cell still remains high stability over 3000 cycles (overpotential, < 79.1 mV) with only ~75.6 mV overpotential after 1500 cycles (Figure 2c). In addition, the cycling stability is further evaluated at low current density (1 and 5 mA cm^{-2}) battery tests and obtained similar results (Figure S37). However, the cycling performance of PVC@Zn anode fluctuates significantly under the same testing procedures (Figure S41). Moreover, the rate performances of the bare Zn and PVC-Zn-AAn-COF@Zn anodes are further compared and examined through the galvanostatic cycle curves at various current densities from 1 to 20 mA cm^{-2} with the capacity of 1 mAh cm^{-2} (Figure 2d and S42). The voltage hysteresis for the PVC-Zn-AAn-COF@Zn anode is kept at a high current density of 20 mA cm^{-2} (low overpotential, ~98 mV), which is much superior to the bare Zn. The cycling performance of the PVC-Zn-AAn-COF@Zn symmetrical batteries is compared with the results of previously reported Zn-metal composite anodes (Figure 2e and Table S3). Notably, the long-term stability of PVC-Zn-AAn-COF@Zn anode at 20 mA cm^{-2} outperforms most other previously reported Zn-metal anodes (Table S3).[3a,6b,11b,13a,19]

Furthermore, the reliability of the PVC-Zn-AAn-COF@Zn anode as commercial electrodes, the large-capacity charge-discharge (5 mAh cm^{-2}) of the symmetrical battery at 5 mA cm^{-2} has been tested (Figure S43). The PVC-Zn-AAn-COF@Zn battery can still maintain excellent cycle stability at 5 mA cm^{-2} (low overpotential, ~37.5 mV). In addition, the PVC-Zn-AAn-COF@Zn electrode displays firm CEs at 20 mA cm^{-2} (Figure S44). The CE is one of the most vital parameters to evaluate the reversibility of Zn plating/stripping, thus asymmetric Zn//Cu and PVC-Zn-AAn-COF@Zn//Cu have been assembled and tested. In bare Zn//Cu cell, the initial CE is just ~77.2% and gradually increases to ~97.7% after 5 cycles, and it fluctuates dramatically after 24 cycles. Notably, the PVC-Zn-AAn-COF@Zn//Cu cell delivers a high initial CE of ~77.6%, and it rapidly increases to 99.3%. Even after 100 cycles, the CE maintains quite stable. Moreover, it delivers only initial voltage hysteresis of ~66 mV, which is lower than that of the Cu electrode (~74 mV), reflecting a larger energy barrier for the nucleation and dissolution of Zn in the phase transition between Zn metal and Zn^{2+} (Figure S44d).[5a,18]

The excellent inhibitory effect and structural integrity of the PVC-Zn-AAn-COF@Zn after cycling tests have been confirmed by SEM images of bare Zn, PVC-AAn-COF@Zn and PVC-Zn-AAn-COF@Zn after 100 cycles (Figure S45). As expected, the bare Zn anode shows giant cracks with massive mossy Zn after 100 cycles of Zn plating/stripping at 20 mA cm^{-2} and PVC-AAn-COF@Zn uneven deposition with serious agglomeration (Figure
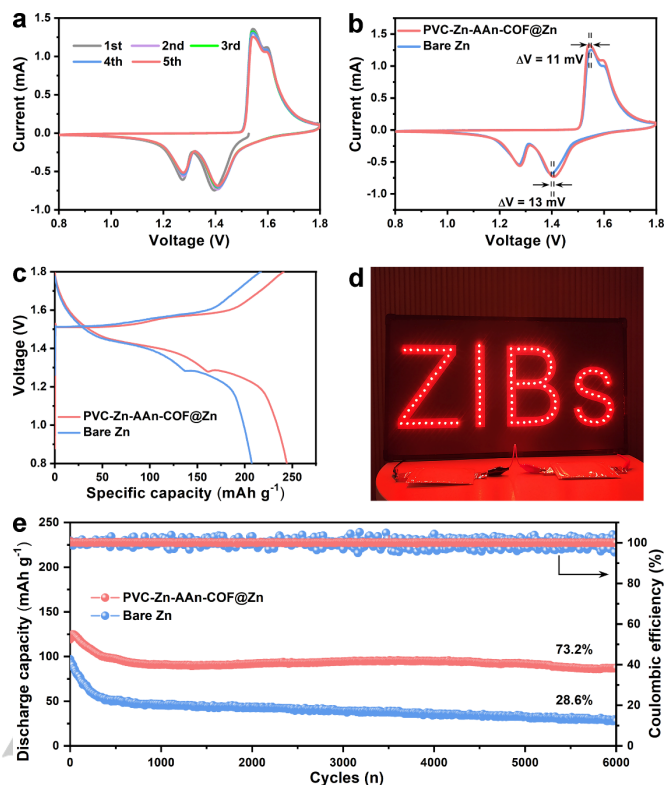

Figure 3. Electrochemical performances of the bare Zn//MnO$_2$ and PVC-Zn-AAn-COF@Zn//MnO$_2$ batteries. (a) CV curves measured from 0.8 to 1.8 V for PVC-Zn-AAn-COF@Zn//MnO$_2$ battery. (b) Comparison of the 5th cycle CV curves of Zn//MnO$_2$ and PVC-Zn-AAn-COF@Zn//MnO$_2$ batteries. (c) Galvanostatic charge-discharge profiles of Zn//MnO$_2$ and PVC-Zn-AAn-COF@Zn//MnO$_2$ batteries at current density of 200 mA g^{-1}. (d) Digital photograph of the flexible battery serving as the energy source to power a LED indicator. (e) Cycling performances of Zn//MnO$_2$ and PVC-Zn-AAn-COF@Zn//MnO$_2$ batteries at current density of 2000 mA g^{-1}.

S45a-f). Noteworthy, no apparent Zn dendrite or protrusions appeared on the PVC-Zn-AAn-COF@Zn surface, indicating the superiority of PVC-Zn-AAn-COF to bare Zn and PVC-AAn-COF (Figure S45g-i).

Besides, the full cell was fabricated by choosing MnO$_2$ as the cathode to prove the feasibility of practical application. In order to evaluate the performance of the full battery, the electrolyte was mixed by 1 M ZnSO$_4$ and 0.1 M MnSO$_4$ solution, in which MnSO$_4$ acted as an additive for the purpose of limiting the dissolution of Mn^{2+} from MnO$_2$ cathode.[11b,13a] The cyclic voltammetry (CV) curves of PVC-Zn-AAn-COF@Zn//MnO$_2$ battery are conducted (Figure 3a). Clearly, the PVC-Zn-AAn-COF@Zn//MnO$_2$ battery demonstrates almost uniform curves in different cycles, showing its excellent reversibility. Besides, the voltage gap between the oxidation-reduction peaks of PVC-Zn-AAn-COF@Zn//MnO$_2$ battery is smaller than that of Zn//MnO$_2$ battery (Figure 3b), exhibiting faster reaction kinetics and lower polarization. The higher performance which was also proved by the galvanostatic intermittent titration technique (GITT) (Figure S46).[7,8d] The result is further confirmed by the galvanostatic charge-discharge curves at 200 mA g^{-1} (Figure 3c and S47a). Besides, the PVC-Zn-AAn-COF@Zn//MnO$_2$ battery exhibits more remarkable cycling stability in comparison with Zn//MnO$_2$ battery at 1000 mA g^{-1} (Figure S47b). Even the current density increases to 2000 mA g^{-1}, PVC-Zn-AAn-COF@Zn//MnO$_2$ battery have a high initial
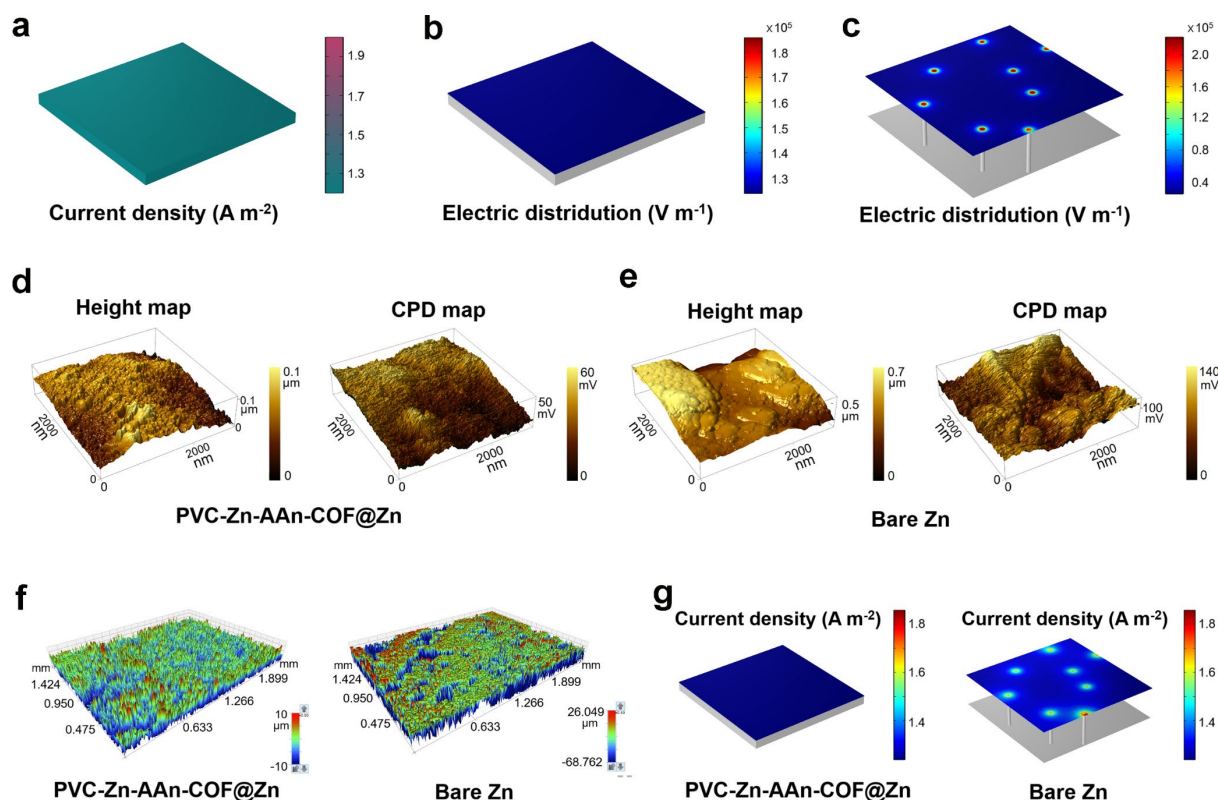
5

RESEARCH ARTICLE

Figure 4. Simulation of current density distribution, AFM and KPFM images of the Zn and PVC-Zn-AAn-COF@Zn anodes. (a) Simulation of the current density distribution for PVC-Zn-AAn-COF@Zn electrode. (b) Models of the relative intensity distributions of localized electric field for PVC-Zn-AAn-COF@Zn anode during Zn nucleation process. (c) Models of the relative intensity distributions of localized electric field for bare Zn anode during Zn nucleation process. (d) AFM images of the PVC-Zn-AAn-COF@Zn. (e) AFM images of the bare Zn foil. (f) 3D laser optical images of PVC-Zn-AAn-COF@Zn and bare Zn anode surface in symmetrical batteries after 100th cycles at 10 mA cm^{-2} with 1 mAh cm^{-2}. (g) Simulation of the current density distribution of the electrolyte at the interface of PVC-Zn-AAn-COF@Zn and bare Zn anode, respectively.

specific capacity (119.3 mAh g^{-1}) than the Zn//MnO$_2$ battery. A high capacity of 90.9 mAh g^{-1} with 100.0% CE of PVC-Zn-AAn-COF@Zn//MnO$_2$ battery after 1000 cycles a is retained, corresponding to capacity retention of 76.2% (Figure 3e). In comparison, the Zn//MnO$_2$ battery can only stabilize in the initial few cycles, after which the specific capacity decays rapidly. In order to prove the excellent dendrite inhibition effect of PVC-Zn-AAn-COF@Zn electrode of PVC-Zn-AAn-COF@Zn//MnO$_2$ full battery after 1000 cycles, the SEM tests of bare Zn and PVC-Zn-AAn-COF@Zn electrode after 1000 cycles at 2000 mA g^{-1} have been tested. The bare Zn anodes show larger dendrites and giant cracks after 1000 cycles at the current density of 2000 mA g^{-1} (Figure S48a-b). Under the same test conditions, the surface of PVC-Zn-AAn-COF@Zn becomes slightly rough and no obvious Zn dendrite or protrusions occurred on the PVC-Zn-AAn-COF@Zn surface (Figure S48c-d), indicating that the PVC-Zn-AAn-COF contributes to guide the uniform deposition of Zn deposition. Besides, the PVC-Zn-AAn-COF@Zn//MnO$_2$ full battery exhibits more excellent rate performance when compared with that of Zn//MnO$_2$ battery (Figure S49). To further certify the application prospects of PVC-Zn-AAn-COF@Zn anode for constructing realistic, smart and high-performance ZABs, we assembled a flexible battery for device demonstration. To create a more realistic scenario, the PVC-Zn-AAn-COF@Zn//MnO$_2$ pouch battery can supply the power for a light emitting diode

(LED) indicator, showing its promising application in portable electronic devices (Figure 3d and S50).

Based on the previously collected results, the uniform Zn deposition and nucleation behaviors of PVC-Zn-AAn-COF@Zn has been further investigated. To simulate the electric field at the anode-electrolyte interface as well as the local current density, the finite element simulation implemented in COMSOL Multiphysics has been applied.[7,18] According to the structure of PVC-Zn-AAn-COF@Zn and bare Zn foil (Figure S51), a simplified 3D optical images model has been established (Figure 4a and S52). The PVC-Zn-AAn-COF@Zn can effectively reduce the local current density, which is superior to the bare Zn anode (Figure 4b and c). According to Sand's time model, the initial growth point of the dendrite would be delayed by lowering the local current density. At the same time, the PVC-Zn-AAn-COF@Zn can provide uniformly distributed electric field and facilitate Zn^{2+} to quickly and homogeneously input the electrode to yield uniform Zn deposition. Due to the uniform electric field formed in the precocious stage and retained during subsequent cycling, Zn^{2+} can be homogeneously deposited on the Zn foil (Figure 4b, S52a and S53a). In contrast, the bare Zn electrode tends to display obviously uneven and individual nucleation sites at the initial state and further evolves into the random Zn deposition and form irregular protuberances because of the poor Zn affinity (Figure 4c, S52b and S53b). These distinct surface geometries and surface potential of Zn foils and PVC-Zn-AAn-COF@Zn are further
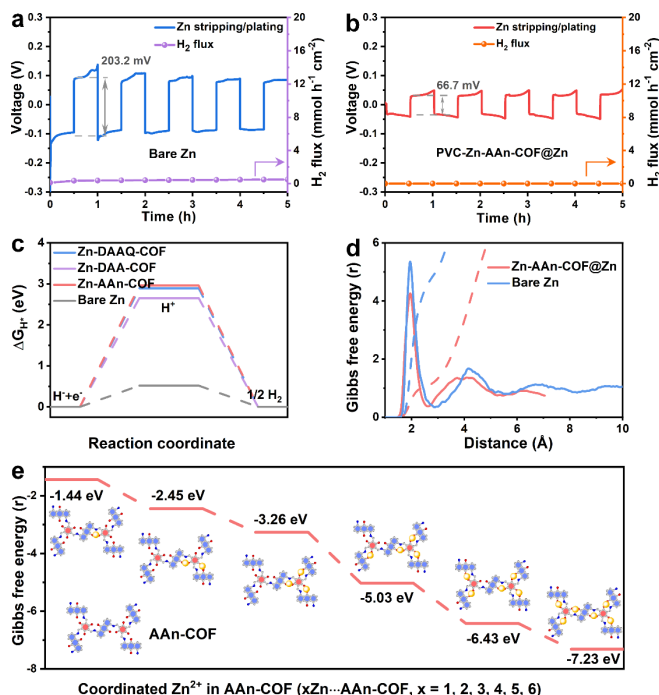
6

RESEARCH ARTICLE

Figure 5. *Ex*-monitoring of H_2 evolution flux for symmetric cells and theoretical simulations. (a) Bare Zn symmetric cell. (b) PVC-Zn-AAn-COF@Zn symmetric cell. (c) DFT calculations to study the ΔG_{H^*} of Zn-AAn-COF@Zn, Zn-DAAQ-COF@Zn, Zn-DAA-COF@Zn and bare Zn. (d) Radial distribution functions plots and the coordination number of Zn-H_2O on Zn-AAn-COF@Zn and Zn surfaces in $ZnSO_4$ electrolyte. (e) Simulation of binding energies with different numbers of Zn^{2+} in Zn-AAn-COF.

verified with the aid of atomic force microscopy (AFM) height tests and Kelvin probe force microscopy (KPFM) potential measurements (Figure 4d and e).[6a,18,20] Initial PVC-Zn-AAn-COF@Zn anode has a relatively flat and uniform surface with an average height of ~100 nm and a low surface potential of ~50 mV. In comparison, the rough surface of Zn anode possesses an average height of ~500 nm and a surface potential of ~100 mV. Besides, the corresponding color of surface roughness from 2D/3D laser optical images exhibits that the surface of PVC-Zn-AAn-COF@Zn foil is smoother after cycling (Figure 4f and S54). In addition, the current density distributions of electrolyte on the electrode surface of the PVC-Zn-AAn-COF@Zn and bare Zn are further simulated by COMSOL Multiphysics (Figure 4g). As expected, the current density distribution of electrolyte on the PVC-Zn-AAn-COF@Zn surface is more uniform than bare Zn.

To accurately quantify the H_2 evolution, a battery-gas chromatography-mass spectrometry (GC-MS) has been utilized to *ex-situ* monitor the H_2 flux during the Zn plating/stripping process at 10 mA cm^{-2} with 5 mAh cm^{-2} (Figure 5a). The H_2 evolution rate of Zn symmetric cell is 0.35 mmol h^{-1} cm^{-2} at 0.5 h and obviously reaches to 0.49 mmol h^{-1} cm^{-2} at 5 h (Figure 5a). In contrast, there is negligible amount of H_2 evolution (0.002 mmol h^{-1} cm^{-2} at 5 h) has been detected in PVC-Zn-AAn-COF@Zn symmetric cell (Figure 5b). In comparison, the H_2 evolution values of PVC-Zn-DAAQ-COF@Zn and PVC-Zn-DAA-COF@Zn symmetric cells deliver 0.0087 and 0.0091 mmol h^{-1} cm^{-2} at 5 h, respectively, proving the superiority of PVC-Zn-AAn-COF@Zn symmetric cell (Figure S55). In theory, to investigate the mechanism of suppressing H_2 evolution reaction, we calculate the Gibbs free energy of H* adsorption (ΔG_{H^*}) for Zn-COF@Zn and

bare Zn. To produce gaseous H_2, inert water should be firstly adsorbed on the surface of the samples, followed by the dissociation process to produce adsorbed H* and OH*. The ΔG_{H^*} value of Zn-AAn-COF@Zn (2.94 eV) is ~6 times higher that of bare Zn (0.52 eV), indicating a weaker H* adsorption ability (Figure 5c). Compared with Zn-DAAQ-COF@Zn and Zn-DAA-COF@Zn anodes, Zn-AAn-COF@Zn anode could also offer a more difficult water dissociation process and consequently a much lower proton supply, thus effectively suppressing the H_2 evolution (Figure 5d). We further calculated the coordination number of Zn-H_2O on the electrode surface by molecule dynamics simulations (Figure 5d and S56).[21] The coordination number of Zn-H_2O on the surface of Zn-AAn-COF (~1) is much lower than bare Zn (~6) by the radial distribution function result (Figure 5d), which represents that Zn-AAn-COF would be more favorable for removing the hydrated molecules on the surface of Zn^{2+} to hinder the by-products formation and competitive H_2 evolution due to the de-solvation effect.[4a,21,22]

In addition, the exact Zn^{2+} storage sites of Zn-AAn-COF during the charge-discharge processes have been identified by the electrostatic potential surface (EPS) method (Figure S57). From the ESP mapping, the regions of more negative values (navy blue) concentrated on the carbonyl groups than -C=N sites, which are considered as highly reactive sites for uptaking Zn^{2+} and tend to be the prime storage sites.[10a] Whereas, Zn-AAn-COF reveals lower EPS value than that of Zn-DAAQ-COF, indicating stronger sites for uptaking the Zn^{2+}.[16c] As such, the quinone redox groups significantly affect the electronic structure and lead to more extensive electron delocalization within the COFs backbone, indicating a higher redox activity of Zn-AAn-COF.[16c,23] Moreover, the active redox centers from the quinoneoxy group are highly reversible to coordinate Zn^{2+} during the Zn^{2+} uptaking process. It is also confirmed that the possible active sites for ion accommodation in Zn-AAn-COF outnumber Zn-DAAQ-COF (Figure S57). Furthermore, we obtained the optimal coordination sites of two Zn^{2+} for AAn-COF through the DFT calculations (Figure S58). According to the experiment results and theoretical calculations of the quinone unit enriched with negative EPS region, the reaction of Zn^{2+} on the surface of Zn-AAn-COF@Zn electrode is a spontaneous reaction process. Specifically, the binding energy with the optimized energy-favored structure of repetitive Zn-AAn-COF units during the multi-step zincation processes has been individually studied by DFT calculations. The results deliver that the negative Gibbs free energy values of Zn-AAn-COF unit are achieved after Zn^{2+} uptaking, indicating that Zn-AAn-COF is able to accommodate a maximum of 6 Zn^{2+} during the hopping process based on the efficient utilization of redox-active groups (Figure 5e).[16b,16c] Given the above results, we surmise that the regulation of the de-solvation, coordination sites, and binding energy in Zn-AAn-COF are the key reasons to prevent H_2 evolution and hinder by-product formation, thus resulting in improving rate capability and cycling stability performances.

Conclusion

In summary, a series of zincophilic COFs (e.g., Zn-AAn-COF, Zn-DAAQ-COF, Zn-DAA-COF) have been applied as model platforms to manipulate the H_2 evolution and Zn^{2+} flux. In general, the H_2-production, qualification or inhibition mechanisms that are closely related to the dendrite-growth have remained a daunting

7

RESEARCH ARTICLE

challenge. In this work, the H_2 evolution has been successfully qualified and studied in these COFs based model platforms. DFT calculation results show that the zincophilic COFs like Zn-AAn-COF has a higher adsorption energy for Zn atoms than that of Zn foil, and the unique pore structure and electrostatic potential distribution of Zn-AAn-COF can effectively remove the Zn solvated water in the bulk electrolyte to avoid H_2 evolution and Zn corrosion. Best of them, the PVC-Zn-AAn-COF@Zn electrode shows remarkably suppressed H_2 evolution in comparison to the bare Zn electrode (0.002 vs 0.49 mmol h^{-1} cm^{-2} in symmetric cell). As a result, the symmetric cells assembled with PVC-Zn-AAn-COF@Zn anode exhibit excellent cycling stability for 3000 cycles with low overpotential (< 79.1 mV) at a high current density of 20 mA cm^{-2} for 1 mAh cm^{-2}, achieving both dendrite-free morphology and negligible H_2 evolution behavior. When coupled with MnO_2 cathode, the assembled PVC-Zn-AAn-COF@Zn//MnO_2 full battery delivers an enhanced cycling stability of up to 6000 cycles at 2000 mA g^{-1}. The performance achieved surpasses almost all other previously reported Zn-metal composite anodes as far as know. Besides, H_2 inhibition and Zn dendrite formation have been intensively studied by DFT calculations and sufficient characterizations, which deliver that these COFs can enhance the energy-barrier of H_2 evolution and homogenize the ion-distribution or electric-filed to achieve high performances. This work might shed fresh light on the exploration of porous crystalline materials in next-generation ZABs.

Supplemental Information includes 58 Figures and 3 Tables

Acknowledgements

Conflict of Interest

The authors declare no conflict of interest.

Keywords: Metal-covalent organic frameworks • Inhibition hydrogen evolution • Suppression the Zn dendrite growth • Homogeneous zinc ion flux

References

[1] a) E. Hu, X.-Q. Yang, *Nat. Mater.* **2018**, *17*, 478-483; b) R. F. Service, *Science* **2021**, *372*, 6545; c) P. Xue, S. R. Liu, X. L. Shi, C. Sun, C. Lai, Y. Zhou, D. Sui, Y. S. Chen, J. J. Liang, *Adv. Mater.* **2018**, *30*, 1804165.

[2] a) X. Wu, X. Ji, *Nat. Chem.* **2019**, *11*, 680-681; b) S. Liu, R. Zhang, J. Mao, Y. Zhao, Q. Cai, Z. Guo, *Sci. Adv.* **2022**, *8*, eabn5097.

[3] a) Z. Yi, G. Chen, F. Hou, L. Wang, J. Liang, *Adv. Energy Mater.* **2020**, *11*, 2003065. b) L. Ma, M. A. Schroeder, O. Borodin, T. P. Pollard, M. S. Ding, C. Wang, K. Xu, *Nat. Energy* **2020**, *5*, 743-749.

[4] a) F. Wang, O. Borodin, T. Gao, X. Fan, W. Sun, F. Han, A. Faraone, J. A. Dura, K. Xu, C. Wang, *Nat. Mater.* **2018**, *17*, 543-549; b) L. Ma, Q. Li, Y. Ying, F. Ma, S. Chen, Y. Li, H. Huang, C. Zhi, *Adv. Mater.* **2021**, *33*, e2007406.

[5] a) H. Yu, Y. Zeng, N. W. Li, D. Luan, L. Yu, X. W. D. Lou, *Sci. Adv.* **2022**, *8*, eabm5766; b) P. Xue, C. Guo, L. Li, H. P. Li, D. Luo, L. C. Tan, Z. W. Chen, *Adv. Mater.* **2022**, *34*, 2110047.

[6] a) R. Zhao, Y. Yang, G. Liu, R. Zhu, J. Huang, Z. Chen, Z. Gao, X. Chen, L. Qie, *Adv. Funct. Mater.* **2020**, *31*, 2001867; b) M. Zhu, J. Hu, Q. Lu, H. Dong, D. D. Karnaushenko, C. Becker, D. Karnaushenko, Y. Li, H. Tang, Z. Qu, J. Ge, O. G. Schmidt, *Adv. Mater.* **2021**, *33*, 2007497; c) Y. Yang, C. Liu, Z. Lv, H. Yang, Y. Zhang, M. Ye, L. Chen, J. Zhao, C. C. Li, *Adv. Mater.* **2021**, *33*, 2007388; d) D. Han, S. Wu, S. Zhang, Y. Deng, C., Cui, L. Zhang, Y. Long, H. Li, Y. Tao, Z. Weng, Q. H. Yang, F. Kang, *Small* **2020**, *16*, 2001736; e) L. Wang, W. Huang, W. Guo, Z. H. Guo, C. Chang, L. Gao, X. Pu, *Adv. Funct. Mater.* **2021**, *32*, 2108533.

[7] L. Hong, L. Y. Wang, Y. Wang, X. Wu, W. Huang, Y. Zhou, K. X. Wang, J. S. Chen, *Adv. Sci.* **2022**, *9*, 2104866.

[8] a) C. S. Diercks, O. M. Yaghi, *Science* **2017**, *355*, 6328; b) H. Xu, J. Gao, D. Jiang, *Nat. Chem.* **2015**, *7*, 905-912; c) Z. Wang, S. Zhang, Y. Chen, Z. Zhang, S. Ma, *Chem. Soc. Rev.* **2020**, *49*, 708-735; d) S. Zheng, D. Shi, D. Yan, Q. Wang, T. Sun, T. Ma, L. Li, D. He, Z. Tao, J. Chen, *Angew Chem. Int. Ed.* **2022**, *61*, 202117511.

[9] D. Ma, H. Zhao, F. Cao, H. Zhao, J. Li, L. Wang, K. Liu, *Chem. Sci.* **2022**, *13*, 2385-2390.

[10] a) Q. Zhao, W. Huang, Z. Luo, L. Liu, Y. Lu, Y. Li, L. Li, J. Hu, H., Ma, J. Chen, *Sci. Adv.* **2018**, *4*, eaao1761; b) D. Wang, Q. Li, Y. Zhao, H. Hong, H. Li, Z. Huang, G. Liang, Q. Yang, C. Zhi, *Adv. Energy Mater.* **2022**, *12*, 2102707.

[11] a) W. Wang, V. S. Kale, Z. Cao, S. Kandambeth, W. Zhang, J. Ming, P. T. Parvatkar, E. Abou-Hamad, O. Shekhah, L. Cavallo, M. Eddaoudi, H. N. Alshareef, *ACS Energy Lett.* **2020**, *5*, 2256-2264; b) Z. Zhao, R. Wang, C. Peng, W. Chen, T. Wu, B. Hu, W. Weng, Y. Yao, J. Zeng, Z. Chen, P. Liu, Y. Liu, G. Li, J. Guo, H. Lu, Z. Guo, *Nat. Commun.* **2021**, *12*, 6606.

[12] L. Cao, D. Li, T. Pollard, T. Deng, B. Zhang, C. Yang, L. Chen, J. Vatamanu, E. Hu, M. J. Hourwitz, L. Ma, M. Ding, Q. Li, S. Hou, K. Gaskell, J. T. Fourkas, X. Q. Yang, K. Xu, O. Borodin, C. Wang, *Nat. Nanotechnol.* **2021**, *16*, 902-910.

[13] a) J. H. Park, M. J. Kwak, C. H. wang, K. N. Kang, N. Liu, J. H. Jang, B. A. Grzybowski, *Adv. Mater.* **2021**, *33*, 2101726; b) J. Zhao, Y. Ying, G. Wang, K. Hu, Y. D. Yuan, H. Ye, Z. Liu, J. Y. Lee, D. Zhao, *Energy Storage Mater.* **2022**, *48*, 82-89.

[14] Z. Wang, J. Huang, Z. Guo, X. Dong, Y. Liu, Y. Wang, Y. Xia, *Joule* **2019**, *3*, 1289-1300.

[15] a) M. Liu, Y.-R. Wang, H.-M. Ding, M. Lu, G.-K. Gao, L.-Z. Dong, Q. Li, Y. Chen, S.-L. Li, Y.-Q. Lan, *Sci. Bull.* **2021**, *66*, 1659-1668; b) C. Guo, M. Liu, G.-K. Gao, X. Tian, J. Zhou, L.-Z. Dong, Q. Li, Y. Chen, S.-L. Li, Y.-Q. Lan, *Angew Chem. Int. Ed.* **2022**, *61*, 202113315; c) M. Lu, Q. Li, J. Liu, F.-M. Zhang, L. Zhang, J.-L. Wang, Z.-H. Kang, Y.-Q. Lan, *Appl. Catal. B: Environ.* **2019**, *254*, 624-633.

[16] a) K. W. Nam, H. Kim, Y. Beldjoudi, T. W. Kwon, D. J. Kim, J. F. Stoddart, *J. Am. Chem. Soc.* **2020**, *142*, 2541-2548; b) M. Yu, N. Chandrasekhar, R. K. M. Raghupathy, K. H. Ly, H. Zhang, E. Dmitrieva, C. Liang, X. Lu, T. D. Kuhne, H. Mirhosseini, I. M. Weidinger, X. Feng, *J. Am. Chem. Soc.* **2020**, *142*, 19570-19578; c) W. Wang, V. S. Kale, Z. Cao, Y. Lei, S. Kandambeth, G. Zou, Y. Zhu, E. Abouhamad, O. Shekhah, L. Cavallo, M. Eddaoudi, H. N. Alshareef, *Adv. Mater.* **2021**, *33*, 2103617; d) Y. Liang, Y. Jing, S. Gheytani, K. Y. Lee, P. Liu, A. Facchetti, Y. Yao, *Nat. Mater.* **2017**, *16*, 841-848; e) Z. Lin, H. Y. Shi, L. Lin, X. Yang, W. Wu, X. Sun, *Nat. Commun.* **2021**, *12*, 4424.

[17] a) J. Hao, X. Li, S. Zhang, F. Yang, X. Zeng, S. Zhang, G. Bo, C. Wang, Z. Guo, *Adv. Funct. Mater.* **2020**, *30*, 2001263; b) S. Jiao, J. Fu, M. Wu, T. Hua, H. Hu, *ACS Nano* **2022**, *16*, 1013-1024.

[18] P. Xue, C. Guo, N. Wang, K. Zhu, S. Jing, S. Kong, X. Zhang, L. Li, H. P. Li, Y. Feng, W. Gong, Q. Li, *Adv. Funct. Mater.* **2021**, *31*, 2106417.

[19] a) S. Park, I. Kristanto, G. Y. Jung, D. B. Ahn, K. Jeong, S. K. Kwak, S. Y. Lee, *Chem. Sci.* **2020**, *11*, 11692-11698; b) Z. Li, L. Wu, S. Dong, T. Xu, S. Li, Y. An, J. Jiang, X. Zhang, *Adv. Funct. Mater.* **2020**, *31*, 2006495; c) G. Zhang, X. Zhang, H. Liu, J. Li, Y. Chen, H. Duan, *Adv. Energy Mater.* **2021**, *11*, 2003927; d) X. Liu, F. Yang, W. Xu, Y. Zeng, J. He, X. Lu, *Adv. Sci.* **2020**, *7*, 2002173.

[20]   W. Zhang, Q. Zhao, Y. Hou, Z. Shen, L. Fan, S. Zhou, Y. Lu, L. A. Archer, *Sci. Adv.* **2021**, *7*, eabl3742.

[21]   F. Ming, Y. Zhu, G. Huang, A. H. Emwas, H. Liang, Y. Cui, H. N. Alshareef, *J. Am. Chem. Soc.* **2022**, *144*, 7160-7170.

[22]   a) Q. Zhang, Y. Ma, Y. Lu, X. Zhou, L. Lin, L. Li, Z. Yan, Q. Zhao, K. Zhang, J. Chen, *Angew Chem. Int. Ed.* **2021**, *60*, 23357-23364; b) L. Cao, D. Li, T. Deng, Q. Li, C. Wang, *Angew. Chem. Int. Ed.* **2020**, *59*, 19292-19296.

[23]   M. Abdul Khayum, G. Meena, V. Vidyanand, H. Arjun, N. Maryam, K. Sushil, A. Matthew, K. Sreekumar, B. Rahul, *Chem. Sci.* **2019**, *10*, 8889-8894.

9

WILEY-VCH

RESEARCH ARTICLE

Entry for the Table of Contents
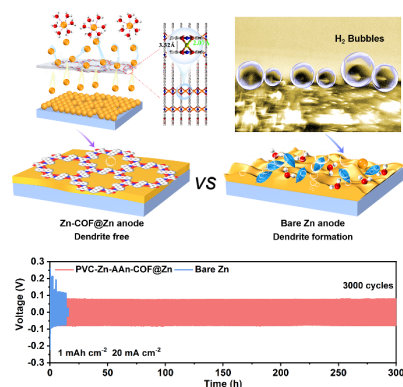
A series of porous Zn-COF@Zn anodes have been fabricated to synergistically manipulate the H_2 evolution and Zn^{2+} flux, during which the closely related H_2 qualification/inhibition and Zn dendrite-growth in zinc-based aqueous batteries have been studied.